RSC Advances

PAPER

View Article Online
View Journal | View Issue

Cite this: *RSC Adv.*, 2025, **15**, 17649

Biomimetic trilayered silk-based electrospun scaffolds for regeneration of dura mater

Maryam Shafiq,[a] Sadia Habib,[a] Hafsah Akhtar,[a] Saamia Naz,[a] Mustafa Özgür Öteyaka,[b] Asma Tufail Shah,[a] Fahad Hussain Alhamoudi,[c] Aqif Anwar Chaudhry,[a] Hamad Khalid*[a] and Ather Farooq Khan*[a]

Dura mater healing is essential to prevent cerebrospinal fluid (CSF) leaks in neurosurgical procedures. Drawing inspiration from the hierarchical structure of native dura mater, we have designed a biomimetic electrospun trilayered scaffold (TLS) utilizing silk fiber to replicate both the structure and function of the original tissue. The electrospun trilayered scaffold comprises three distinct layers: a skull-facing layer constructed from silk fibroin combined with strontium-doped bioactive glass, a gradient inert polyurethane middle layer and a brain-facing layer consisting of polyurethane infused with oregano essential oil. For the first time, oregano essential oil is used in dural substitute to impart potential antibacterial properties. The physicochemical properties of TLS were systematically evaluated using Fourier-transformed infrared spectroscopy (FTIR), scanning electron microscopy (SEM), microcomputed tomography (micro-CT) and thermogravimetric analysis. The nanoscale architecture was verified through SEM while micro-CT analysis provided additional insights into the fibrous surfaces of the trilayered scaffold. Surface wettability tests revealed that the wetting characteristics were comparable to those of the native dura mater, with the brain-facing layer exhibiting hydrophobic properties conducive to water-tight dural closure and the skull-facing layer presenting hydrophilic properties favorable for cell adhesion. After immersion in phosphate-buffered saline (PBS) for 28 days, the TLS showed a degradation rate of 13%. Furthermore, the results show that TLS was porous (60%) and demonstrated improved swelling in PBS. The addition of OEO improved the antibacterial potential; the TLS exhibited 80% antibacterial activity against *Escherichia coli* after 48 hours. Furthermore, the fibroblast cell line was exploited to assess the biological properties of TLS. Cell culture results indicated that TLS promoted NIH3T3 proliferation in the 3D microenvironments and was non-toxic. Similarly, live/dead and migration assay results further confirmed the biocompatibility of TLS with increased cell viability and 99% wound closure after 24 hours. Overall, we were able to manufacture a trilayered scaffold that architecturally mimics the native structure of dura mater.

Received 11th February 2025
Accepted 14th May 2025

DOI: 10.1039/d5ra00986c

rsc.li/rsc-advances

1 Introduction

The dura mater is a tough, fibrous tissue that forms the outermost layer of the three meninges encasing the brain and spinal cord which supports and covers the dural sinuses and facilitates the transport of blood from the brain back to the heart.[1] Dura mater can be damaged or shrink due to tumor invasion, cerebrovascular disease, traumatic brain injury, craniocerebral tumor and cerebral or spinal operative procedures.[2,3] Any damage to dura mater leads to CSF leakage which results in serious complications such as brain swelling, cranial and spinal infections, meningitis, epilepsy, seizures and pseudomeningocele.[4,5] So, water-tight dural closure has clinical significance because once dura mater is ruptured or incised, it needs to be repaired with a graft replacement as it is unable to heal itself and causes the CSF to flow into extradural space followed by serious neurological complications.[6,7] Small dural defects can be repaired by direct suturing but when dural defect is large, dural substitutes are required to repair them.[8]

Anatomical examination shows that cranial dura mater is a trilayer structure. The outermost is the skull-facing periosteum layer which is 2 μm thick, containing nerves, blood vessels, fibroblasts, collagen and elastin fibers.[9] The middle layer, fibrous dura, is 400 to 1000 μm thick, based on both the location and age of the patient. The innermost is the meningeal layer whose thickness is approximately 8 μm and contains cells that conform to the arachnoid trabeculae.[10–12] Kegel reported that the average thickness of human dura mater is 1.06 ± 0.22 mm.[13]

[a]*Interdisciplinary Research Centre in Biomedical Materials (IRCBM), COMSATS University Islamabad, Lahore Campus, Defence Road, off Raiwind Road Lahore, Pakistan. E-mail: atherfarooq@cuilahore.edu.pk*

[b]*Eskişehir Vocational School, Electronic and Automation, Mechatronic Program, Eskişehir Osmangazi University, Eskisehir, 26250, Türkey*

[c]*Department of Allied Dental Health Science, College of Medical Science, King Khalid University, Abha 62529, Kingdom of Saudi Arabia*

In clinical and research practices, various biological and synthetic dural substitutes exist, but their use is limited by issues like donor availability, infection risks, and lack of mechanical strength.[14–18] Combining natural and synthetic materials can enhance biocompatibility and durability. Natural polymers are gaining attention in tissue engineering and regenerative medicine.[19,20] Silk fibroin (SF) stands out due to its excellent mechanical properties, biocompatibility, controlled degradation, and low inflammatory response.[21–25] Polyurethane, a synthetic polymer, is well-known for its flexibility and self-healing abilities.[26] Additionally, incorporating ceramics like bioactive glass into polymeric systems promotes tissue and bone regeneration.[27]

The goal of our study is to develop a trilayer electrospun scaffold as a novel dural substitute that can mimic the actual structure of dura mater. For this purpose, the brain-facing layer is prepared which acts as a barrier to prevent CSF leakage and brain tissue adhesion. A middle inert layer is introduced to provide enhanced mechanical strength to the synthetic scaffold. Skull facing layer is fabricated using natural protein – silk fibroin which promotes the native dural healing process by supporting proliferation, cell growth, migration and cell-to-matrix substance exchange, along with tissue adhesion. For the first time, essential oil is used in dural substitute to impart potential antibacterial and anticancer property. Oregano essential oil is added to the brain facing polyurethane layer with the purpose of suppressing the progression of cancer as it possesses carvacrol, a potent antitumor agent. Strontium doped bioactive glass is selected to confer the osteogenic property to the skull facing layer that will help the fusion of this layer to the skull. In this study, a trilayered electrospun scaffold was synthesized and surface morphology, porosity, density, swelling ratio, thermal stability, water absorption and *in vitro* degradation of the scaffolds were studied. The *in vitro* cell proliferation, cell viability and wound healing in the presence of these materials was further investigated.

2 Materials and methodology

2.1 Chemicals reagents

Silk cocoons (Changa Manga Forest, District Kasur, Punjab, Pakistan), hexafluoro isopropanol (TCI), dimethyl formamide (Scharlau), tetrahydrofuran (EMPLURA), sodium carbonate (Scharlau), strontium doped bioactive glass (Sr-BG) (Donated by Dental Group of IRCBM), polyurethane (PU-Z3A1) (Donated by Soft Tissue Engineering Lab of IRCBM), oregano essential oil (PACS), absolute ethanol (EtOH) (Merk), silver nitrate (Sigma-Aldrich), calcium chloride (Daejung), phosphate buffer saline tablets (bioWORLD), agar (Biolab), fetal bovine serum (Sigma), penicillin streptomycin (Biowest), trypsin EDTA (Gibco), DMEM (Gibco), Alamar blue (Alamar BioSciences, Sacramento, CA). All the chemicals used were of analytical grade and used without further purification.

2.2 Preparation of pure freeze-dried silk fibroin scaffolds

Silk cocoons from *Bombyx mori* were degummed to remove glue-like sericin as this protein induces an immunogenic response if applied as a biomaterial. Silk cocoons were cut into small pieces and boiled in deionized water containing 0.02 M Na_2CO_3 for 30 minutes with constant stirring to promote the dissolution of the silk fibers. The degummed silk was washed with deionized water thrice to remove residual sericin. Pure SF was spread on filter paper for drying at room temperature for 24 hours. For the synthesis of silk fibroin solution, degummed fibers were dissolved in a ternary solution system of $CaCl_2$: EtOH : H_2O (1 : 2 : 8). Anhydrous $CaCl_2$ (11.098 g) was dissolved in deionized H_2O (14.4 mL), followed by the addition of 2.25 g of degummed SF. The solution was gently stirred to promote the dissolution of SF by adding EtOH (9.214 mL) and kept in an oven for 3 hours at 70 °C. The solution was dialyzed using cellulose dialysis membrane (MWCO 12 400 kDa) for over 72 hours. Water was changed at the interval of 1, 4, 8, 16 and 24 hours and the solution was centrifuged at 4000 rpm for 20 minutes to remove impurities, maintaining the temperature of 4 °C. Transparent SF supernatant was collected and subsequently freeze-dried for further use in the synthesis of desired electrospun scaffolds.[28]

2.3 Preparation of skull facing layer

For electrospinning, 10% (w/v) SF solution was prepared in 1,1,1,3,3,3-hexafluoro-2-propanol (HFIP) by dissolving 2 g freeze-dried SF in 20 mL HFIP. The solution was mixed under constant magnetic stirring at room temperature until a homogenous clear solution was obtained, and then electrospun to prepare SF control (SFC). For the synthesis of skull facing layer (SFL), 10% Sr-BG was added to the SF solution. To enhance the proper dispersion of bioactive glass in SF solution, Tween 20 was used as an emulsifier. For this purpose, Sr-BG was treated with 10% w/v solution of Tween 20. Afterwards, SF/Sr-BG suspension was prepared by adding 200 mg of the treated Sr-BG to 20 mL homogenous solution of SF. Sr-BG was added slowly under continuous stirring to avoid agglomeration and electrospun to SFL.

2.4 Preparation of gradient inert layer

Aromatic biomedical grade PU-Z3A1 was dissolved into DMF/THF in the volumetric ratio of 70/30 to prepare a solution of 15% w/v concentration. PU-Z3A1 crystals were added slowly to the solvent mixture under constant magnetic stirring at 75 rpm. The solution was stirred overnight to obtain a homogenous mixture for the electrospinning of PU control (PUC) and gradient inert layer (GIL).

2.5 Preparation of brain facing layer

To prepare brain facing layer (BFL), a 5% w/w concentration of OEO was selected with respect to the quantity of PU. OEO was added dropwise to THF as it has ability to dissolve OEO. DMF and PU-Z3A1 crystals were added slowly to the mixture of THF and OEO under constant magnetic stirring at 75 rpm and stirred overnight at room temperature to obtain a crystal-clear solution and electrospun to prepare BFL.

2.6 Synthesis of trilayer electrospun dural substitute scaffolds

2.6.1 Electrospinning. Trilayered scaffolds were prepared by layer-by-layer electrospinning of SF/Sr-BG, PU and PU/OEO respectively. SF/Sr-BG suspension was electrospun by adding into a 20 mL plastic syringe, fitted with stainless steel needle and loaded into automatic syringe pump. Fibers were collected onto an aluminum foil covered drum that was rotating with the speed of 200 rpm to obtain fibers with the random orientation in a closed chamber, where the temperature was maintained at 45 °C. For GIL, a programmable syringe pump was used for the delivery of PU-Z3A1 solution. Random fibers of GIL were deposited on the SF/Sr-BG layer to act as a barrier. To prepare BFL, PU/OEO solution was electrospun on the GIL keeping drum speed 5000 rpm to obtain highly aligned fibers. The thickness of the scaffolds was controlled by adjusting the relative flow rates of each polymer during the electrospinning of the trilayer electrospun dural scaffold (TEDS). All the fabricated scaffolds were vacuum-dried to remove residual solvents at 37 °C. Parameters used in preparing electrospun scaffolds are given in Table 1.

3 Characterization

3.1 FTIR spectroscopy

FTIR spectra were obtained on Thermo Nicolet Scientific-6700 using smart iTR diamond Attenuated total reflection (ATR) mode in the IR range of 4000 cm^{-1} to 400 cm^{-1}. Spectra of all the materials were taken with the scan range of 8 cm^{-1} and a total of 256 runs were performed to determine the specific functional groups against distinctive peaks of the spectra.

3.2 Scanning electron microscopy (SEM)

To determine the surface morphology, fiber alignment and additive distribution, scaffolds were coated with gold and then imaged using a ThermoFisher SCIENTIFIC scanning electron microscope at 5 kV by employing SE (topography) and BSE (phase contrast) modes at a magnification range of 1000*x*–10 000 00*x*. Average fiber diameter and size distribution of each scaffold was determined using Image-J (V 1.54) software on SEM images. For calculating the average fiber diameter, 30 random fibers of each image and 5 points of each fiber were selected to ensure accuracy by applying Gaussian calculation.

3.3 Thermogravimetric analysis

The fabricated trilayer electrospun dural substitutes (TEDS) was analyzed using TGA (Thermogravimetric Analysis) in PerkinElmer. The 10 ∼ 15 mg of sample was subjected to TGA at 10 °C min^{-1} within a temperature range of 30 °C to 800 °C.

3.4 Micro computed tomography (μCT)

The micro computed tomography (μCT) images for TLS were taken using Bruker SKYSCAN 1272. Micro CT images were taken at 70 μA at 25 kV. The pixel size was 9 μm and the rotation step was 0.6°. The images were reconstructed with the NRecon BRUKER reconstruction software.

3.5 Contact angle measurements

Scaffolds were cut into 2 cm × 2 cm sizes and examined by Young Laplace analysis mode using Biolin Scientific Attention Theta measurement. A drop of ultra-pure water (4 μL) was subjected on the surface of the scaffolds and the angle was measured instantly within the 5 seconds of water interaction with the scaffold. Analysis was made on triplicate samples of each scaffold to measure the average contact angle. Drop profile was viewed using telescope goniometer and the images were collected using software attached to the instrument.

3.6 Density measurement

Samples of 2 cm × 2 cm size were analyzed by Quantachrome, Pentapyc 5200e TEMP by purging nitrogen gas in a combined cell pressurization mode. The target pressure was 19 Psi and 6 maximum number of runs were applied giving an average of 3 runs, keeping the temperature 25 °C.

3.7 Porosity measurement

All the samples were dried to a constant weight (W_1). The study was performed in triplicates. Sample scaffolds were dipped in absolute ethanol and *n*-hexane for 1 hour and the wet weight of the samples were noted as W_2. Porosity was measured using the following expression:

Table 1 Parameters of electrospinning

Layer	Composition	Solvent	Voltage (kV)	Feed rate (mL h^{-1})	Distance (cm)	Drum speed (rpm)	Needle (gauge)	Temperature (°C)
SFC	10% SF	HFIP	17	0.3	12	200	18	45
SFL	10% SF + 10% Sr-BG	HFIP	17	0.3	12	200	18	45
PUC	15% PU-Z3A1	DMF/THF (70/30 v/v)	18	0.5	15	5000	20	25
GIL	15% PU-Z3A1	DMF/THF (70/30 v/v)	18	0.5	15	200	20	25
BFL	15% PU-Z3A1 + 5% OEO	DMF/THF (70/30 v/v)	18	0.5	15	500	20	25

$$\text{Porosity (\%)} = [W_2 - W_1/W_2] \times 100$$

3.8 Swelling ratio measurement

All the samples were cut into similar dimensions with equal weights and dried to a constant weight (W_d). Then the dried samples were immersed into freshly prepared PBS solution (7.4 pH), and placed in a shaker at 37 °C. At 24- and 48 hour intervals, samples were taken out, gently tapped on a filter paper to remove excess water, and weighed (W_s). Mean value of the samples were calculated by taking the average of the triplicates. The following equation was used to evaluate the swelling ratio:

$$\text{Swelling ratio (\%)} = [W_s - W_d/W_d] \times 100$$

3.9 *In vitro* degradation studies

To model the degradation profile of the prepared scaffolds, samples of 10 mg (W_o) were immersed in PBS solution, and incubated in a shaker for 3, 7, 14, 21 and 28 days at 37 °C. On the day of completion of the study, the scaffolds were washed with deionized water thrice to avoid any possibility of the presence of salt ions absorbed on the sample surface, and then vacuum dried to remove moisture and dry weight was taken as W_t. The study was carried out with triplicate samples. Following equation was used to evaluate percentage degradation:

$$\text{Degradation (\%)} = (W_o - W_t/W_o) \times 100$$

3.10 Antibacterial study

Antibacterial activity of the scaffolds containing Sr-BG and OEO was examined against *E. coli* using the disk diffusion and broth dilution method. For disk diffusion method, all scaffolds were cut into similar shapes with equal weights (10 mg) and were sterilized by employing UV for 30 minutes before the experiments. Prepared 100 μL bacterial culture was streaked onto the agar plate using a sterile cotton swab and scaffolds were placed with the help of sterile forceps and incubated for 24 hours. Zone of inhibition was determined in millimeter (mm) and a commercial drug was used for comparison. The studies were carried out with triplicate samples. In the broth dilution assay, a series of broth dilutions were prepared to pick a certain amount of bacterial culture. The adjusted inoculum was then dispensed into the 24-well plate, 2 mL per well. The scaffolds were placed in the inoculated plates that were subsequently covered with a sealing parafilm and then incubated in a shaker at 37 °C. Each plate included a positive control having no antibiotic and a negative control (nutrient broth). After 24 and 48 hours of incubation, the growth of the bacteria was determined using a microplate reader (MPR) between 550–650 nm UV wavelength.

$$\text{\% Bacterial inhibition} = [(A_c - A_t)/A_c] \times 100$$

where A_t is the average of absorbance value at 600 nm and A_c is the average value of absorbance of control at 600 nm.

3.11 Cell viability assay

The viability of NIH/3T3 fibroblast cells, which was purchased from American Type Culture Collection (ATCC® CRL6442™) on the composite scaffolds was evaluated using the Alamar blue assay which is a colorimetric assay. 5000 cells were seeded onto the scaffolds in a 96-well plate and incubated in a humidified incubator at 37 °C with 5% CO_2. Cells without any scaffold were taken as a positive control. Readings of Alamar blue were taken on days 1, 4 and 7 for all samples. For each reading, 100 μL of Alamar blue reagent was added to the well and incubated for two hours and thirty minutes. The absorbance was measured at 575 nm using a Microplate reader (Labtech LT4500).

3.12 Live dead assay

Calcein AM, DAPI and propidium iodide were used for this assay. 5×10^4 cells were seeded on the surface of each scaffold under sterile conditions. The samples were incubated in 5% CO_2 humidified incubator at 37 °C for 30 minutes to facilitate adhesion of cells. This was followed by adding complete media. The scaffolds were further incubated for 48 hours. After 48 hours, cells were fixed with 4% paraformaldehyde (PFA) followed by washing with different grades of ethanol (30%, 50%, 70% and 100%). Calcein AM, DAPI and propidium iodide (4 μM) were added to each scaffold and after staining, Olympus BX51 fluorescent microscope was used for imaging.

3.13 Scratch assay

To evaluate the cell migration in the presence of scaffolds in comparison to the control, *in vitro* wound healing scratch assay was performed. NIH3T3 fibroblasts were cultured in a 6 well plate and incubated at 37 °C until they achieved 80% confluency. A vertical scratch was created in the cell monolayer using a sterile micropipette tip. Initial pictures at 0 h were taken right after the scratch was made. The pre-sterilized scaffolds were placed in each well and further images were taken at 4 h, 8 h, 16 h and 24 h with an inverted fluorescent microscope. The scaffolds were placed onto the scratch area, and their influence on fibroblast migration into the scratched area was assessed to determine scaffold-induced enhancement of wound closure. The scratch area was measured from images using Image J software and % wound contraction was determined using the following formula:

$$\text{\% Wound contraction} = (\text{wound area (0 h)} - \text{wound area (}\times\text{h)} / \text{wound area (0 h)}) \times 100.$$

3.14 Statistics

All the experimental results were expressed as the mean ± standard deviation. A series of two-way ANOVA was performed using GraphPad Prism (GraphPad Software, Version 9.00) to evaluate the significant difference. Tukey's multiple

comparison test was performed to evaluate the statistical differences in the fabricated scaffolds. For all analyses, the p values were defined as: $p < 0.05$ (*), $p < 0.01$ (**), $p < 0.001$ (***) and $p < 0.0001$ (****).

4 Results and discussion

4.1 FTIR spectroscopy

FTIR spectroscopy was used to investigate interactions between functional groups in composite scaffolds (Fig. 1). The spectra showed a peak for the amide I of silk fibroin (SF) at 1650 cm^{-1}, linked to C═O bond stretching and bands between 1550 to 1520 cm^{-1} corresponding to amide II, indicating –NH bending and –CN stretching. Intense peaks at 1220–1110 cm^{-1} were attributed to amide III interactions. A band at 3291 cm^{-1} confirmed the presence of SF, displaying N–H and O–H stretching.[29] The bioglass (BG) peak was identified at 1055 cm^{-1}. No significant changes in peaks occurred when SF and BG were combined, suggesting a lack of chemical interaction due to SF's stable beta sheets and random coils.[30] Polyurethane showed a broad N–H stretching peak at 3322 cm^{-1}, an aliphatic methylene group peak at 2860 cm^{-1} and further peaks corresponding to C═C and C═N around 1530 cm^{-1}.[31] For oregano essential oil (OEO), C–H stretching and other distinct peaks were noted, but no significant changes were observed in trilayered scaffolds, except for slight intensity variations attributed to physical interactions. The low amounts of BG and OEO likely resulted in undetectable specific peaks in the TLS.[32]

4.2 Scanning electron microscopy

Scanning electron microscopy (SEM) was utilized to analyze various aspects of the scaffold materials, including surface morphology, fiber orientation and diameter, and distribution as shown in Fig. 2(a–h). These characteristics are crucial for influencing cell attachment, proliferation, and migration, which are essential for tissue growth. In the case of the SF scaffold, rough, porous, and interconnected fibers with random orientation were observed.[33] The average diameter of fibers of pure SF scaffolds was 855 nm. The addition of BG led to a slight decrease in fiber diameter (814 nm) in skull facing layer due to enhanced solution conductivity. The gradient inert layer and brain facing layer scaffolds exhibited uniform, dense, and continuous fibers with minimal change in diameter, where the GIL and BFL showed an average diameter of 513 nm and 602 nm respectively. OEO was evenly dispersed within and on the surface of the fibers, forming tiny white spheres due to the low affinity of oil with the polymer. This suggests physical interaction between the two materials. Additionally, OEO reduced the porosity of the PU scaffold.[34] The aligned fiber architecture of the brain facing layer scaffold was designed to provide physical guidance cues for regenerating cells, promoting cell alignment and guiding nerve growth. In the case of TLS, the SFL retained its characteristic properties, while the brain facing layer exhibited fiber bundles, further reducing porosity and acting as a water barrier surface to prevent cerebrospinal fluid leakage. Furthermore, cross-section analysis showed that all three layers were physically attached without any chemical bonding.

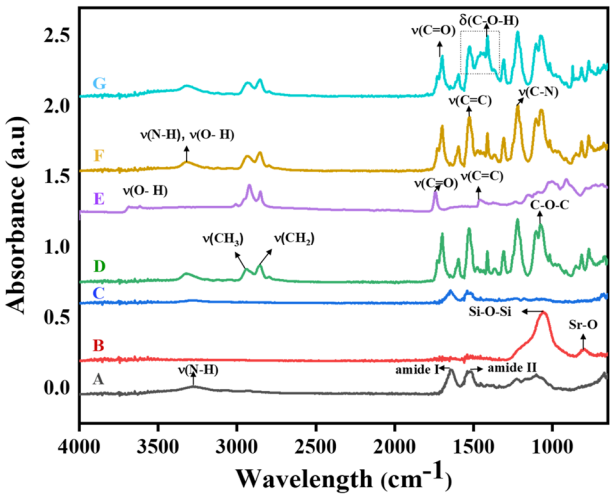

Fig. 1 FTIR spectra of (A): SFC, (B): BG, (C): SFL, (D): GIL, (E): OEO, (F): BFL, (G): TLS. Fourier-transform infrared (FTIR) spectra of the trilayered scaffold (TLS) and its individual components, illustrating the characteristic functional groups.

4.3 Thermogravimetric analysis

To assess the thermal stability of the trilayered scaffold, thermogravimetric analysis was conducted to monitor the rate of weight loss during a controlled heating process, extending from 23 °C to 800 °C. The results, illustrated in Fig. 3, reveal the intricate mass loss patterns of TLS throughout this temperature range. Initially, the TLS scaffold underwent a weight reduction in the first stage, characterized by a 7% loss between temperatures of 60 °C and 170 °C. This initial mass decrease can be attributed primarily to the evaporation of moisture trapped within the scaffold structure.[35] Progressing to the second stage, which spans from 170 °C to 270 °C, there was an additional 3% decline in mass. This slight weight loss is likely linked to the thermal degradation of the oregano essential oil (OEO) incorporated within the scaffold.[36] In the next phase, occurring between 270 °C and 340 °C, the scaffold experienced a significant mass loss of 18.98%. This substantial reduction may be primarily associated with the degradation of silk fibroin (SF), a critical component of the trilayered structure.[35] Further thermal decomposition was observed in the fourth stage, taking place between 340 °C and 450 °C, during which the scaffold exhibited a notable mass loss of 27.29%. This phase of degradation may be attributed to the breakdown of polyurethane (PU).[37] Finally, in the last stage of thermal degradation, spanning from 500 °C to 600 °C, the TLS scaffold showed a 10.53% reduction in mass. This final weight loss is likely due to the degradation of bioactive glass (BG) within the scaffold.[38]

4.4 μCT analysis

Micro-computed tomography (μCT) has become a widely used technique for evaluating and visualizing bone architecture and

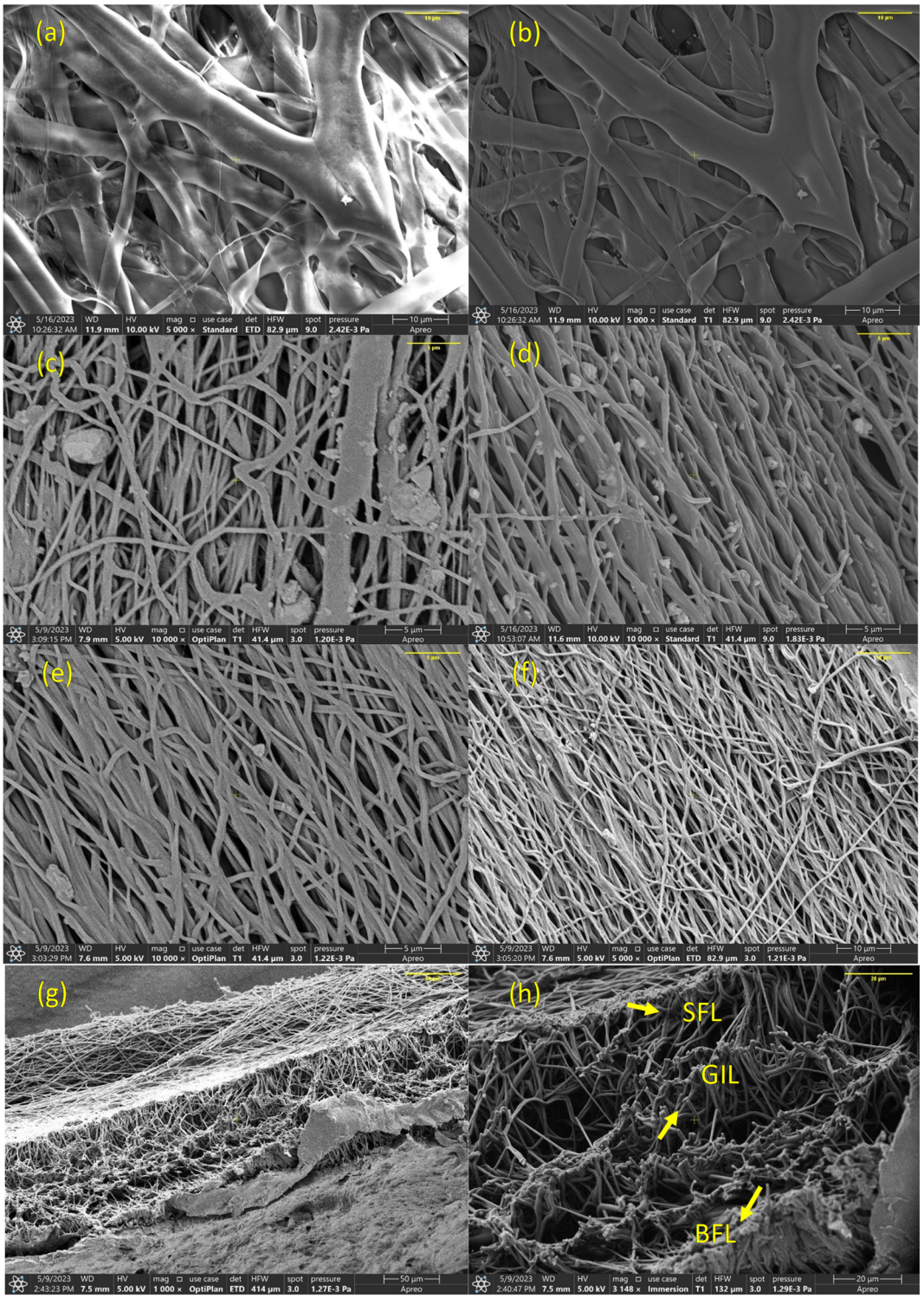

Fig. 2 (a) Pure electrospun SF with AD 855 nm (b) SFL scaffold with AD 814 nm (c) GIL scaffold with AD 531 nm (d) BFL scaffold with AD 602 nm (e) SFL of TLS electrospun scaffold with AD 712 nm (f) BFL of TLS electrospun scaffold with AD 531 nm (g and h) Cross section of TLS.

soft tissues.[39] It allows researchers to examine the three-dimensional structure of tissues. Micro-CT images of the TLS scaffold were observed using a micro-CT system. 3D models were defined from the volume reconstruction of the acquired 2D set of images. Reconstruction was carried out with NRecon software. The μCT images reveal the distinct three layers of the TLS scaffolds. The Fig. 4 shows the microCT images of TLS scaffold. The electrospun fiber bundles can be clearly seen in the micro-CT images with the blue crystals showing the BG particles. Fiber bundles are visible in the skull facing layer (SFL).

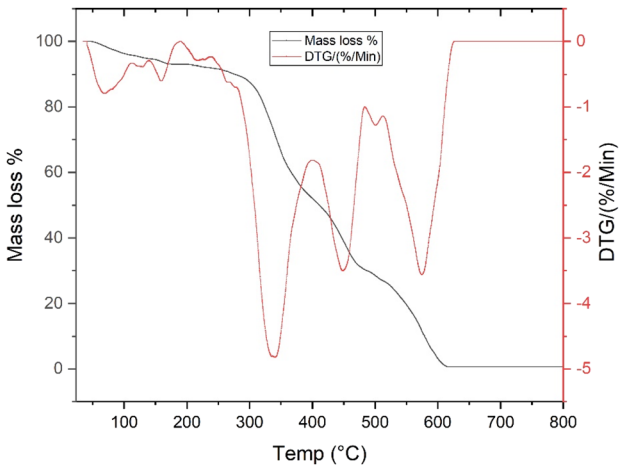

Fig. 3 Thermogravimetric analysis (TGA) and derivative thermogravimetry (DTG) curves of the trilayered scaffold (TLS), illustrating thermal stability and compositional transitions from 23 °C to 800 °C.

4.5 Contact angle measurement

The contact angle measurements of scaffolds were taken to assess their hydrophobicity and hydrophilicity. The pure silk fibroin (SF) scaffold had a contact angle of 76° as shown in Fig. 5. Adding bioactive glass (BG) decreased the contact angle to 72° due to the hydrophilic nature of BG and increased surface area, resulting in more interaction sites for water molecules.[40] The contact angle of the polyurethane (PU) scaffold was 93°, indicating its hydrophobic nature, which increased to 102° with the addition of OEO, a highly hydrophobic substance.[41] The wettability of the composite scaffold showed minimal alteration in properties. The brain facing side of TLS had a contact angle of 97°, maintaining a hydrophobic property suitable for watertight dural closure. The decreased wettability of the brain facing layer could inhibit cancer cell growth, while the contact angle of skull facing layer (71°) was similar to the control (72°), supporting earlier studies that an increase in surface hydrophilicity can enhance cell adhesion.[42] This indicates that incorporating BG into the scaffold may also help improve the scaffold's hydrophilic properties, thus supporting cell attachment.[43]

4.6 Density measurement by pycnometer

Porous polymer scaffolds are essential for promoting tissue regeneration as they provide a framework for cellular attachment and extracellular matrix synthesis. The density of electrospun scaffolds affects their porosity and pore size, which in turn impacts cell infiltration, proliferation, and viability.[44] Achieving the right balance between scaffold porosity and density is crucial for specific applications. While higher scaffold density is associated with increased mechanical strength, higher porosity creates a more favorable biological environment. Therefore, it is important to establish a careful equilibrium between porosity and density to optimize the scaffold's

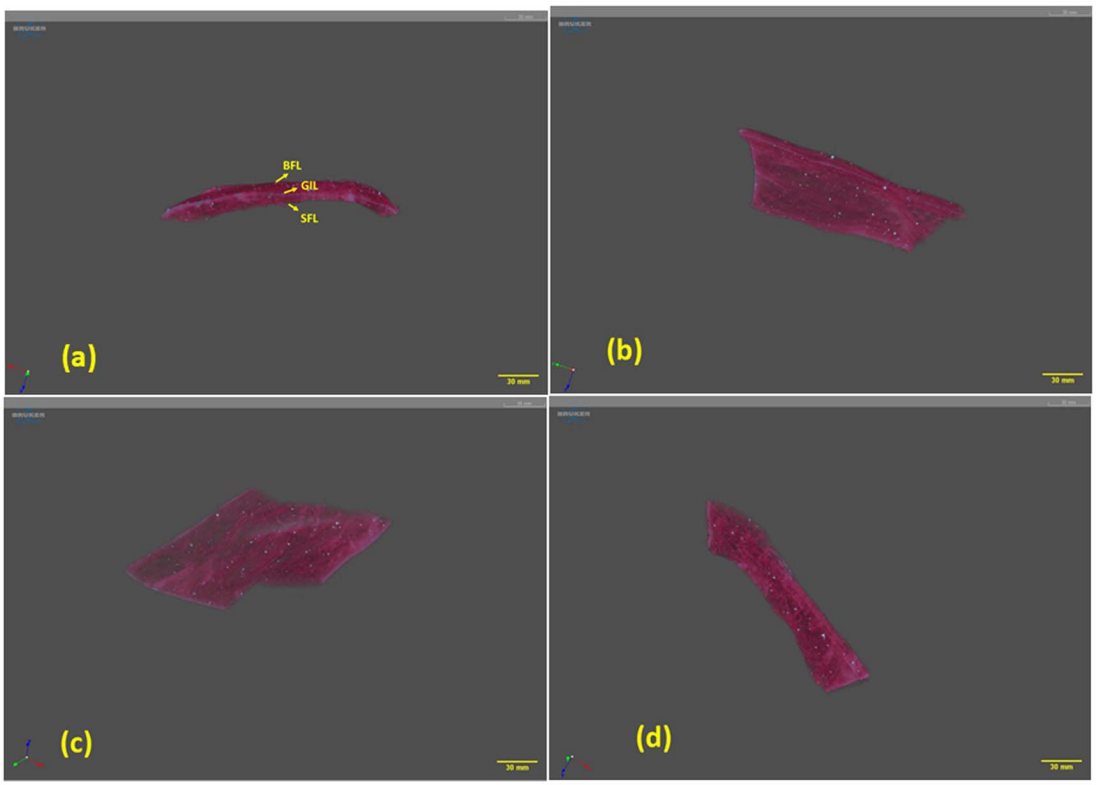

Fig. 4 Micro-CT images of the trilayered scaffolds showing internal morphology and structural organization. The scans reveal the layer-specific architecture of the trilayered scaffold. Each layer is distinguishable based on its microstructural features, reflecting the successful fabrication of the trilayered design. Scale bars are included for reference.

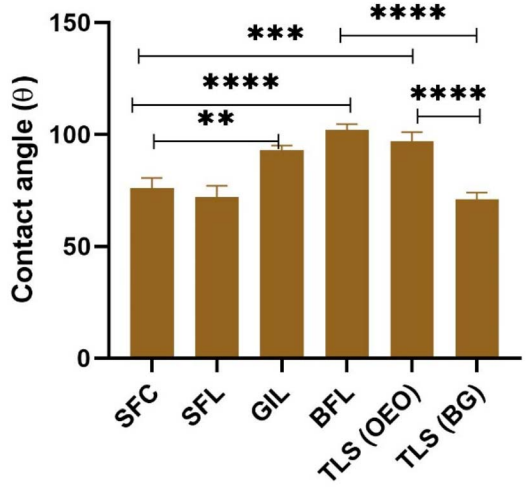

Fig. 5 Contact angle measurements of individual scaffold components and the trilayered scaffold (TLS) to evaluate surface wettability. Error bars represent standard deviation ($n = 3$).

performance for its intended purpose.[45,46] To assess the effect of density on porosity, the average density of all the scaffolds was calculated using a pycnometer (Fig. 6). The inclusion of bioactive glass in the silk fibroin scaffold reduced its density, increasing its porosity and potentially promoting cell growth. This is likely due to the lower density of bioactive glass compared to silk fibers. Similarly, the addition of oregano essential oil to polyurethane scaffolds increased the scaffold's density. Additionally, the combined structure of top and bottom layers of the scaffold showed a slight change in average density, with TLS displaying denser behavior due to the presence of inert layers in between. Overall, stacking layers resulted in a more compact structure, increasing density and reducing porosity while still fulfilling the intended purpose of the composite scaffold.

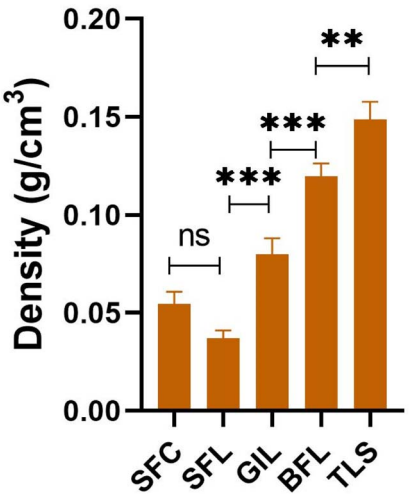

Fig. 6 Average density measurements of individual and composite electrospun TLS scaffold determined using a pycnometer. Error bars represent standard deviation ($n = 3$).

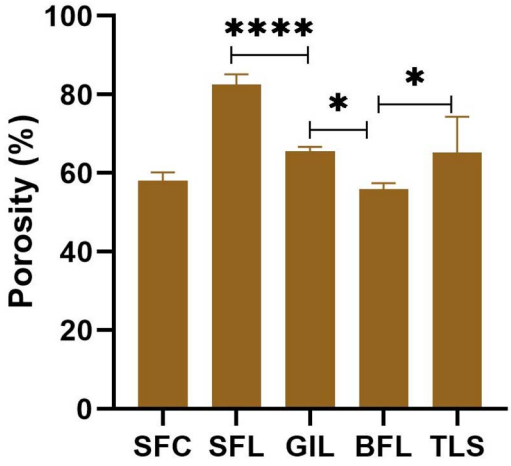

Fig. 7 % Porosity measurements of electrospun scaffolds in absolute ethanol. Error bars represent standard deviation ($n = 3$).

4.7 Porosity measurement

Porosity is an important factor to consider when evaluating the characteristics of biomaterials, particularly for scaffolds, as their porous nature facilitates the diffusion of water and nutrients. The porous structure of a scaffold supports cell attachment, proliferation, migration, and distribution.[47] The porosity of the scaffolds was determined by measuring them in absolute ethanol (Fig. 7) and *n*-hexane (Fig. 8). It was observed that the porosity was higher in absolute ethanol compared to *n*-hexane due to differences in their properties, such as polarity and viscosity. The faster diffusion of ethanol into the scaffold resulted in higher porosity. For example, the porosity of SF was approximately 58% in absolute ethanol and 45% in *n*-hexane. Similarly, SFL demonstrated porous characteristics with values of 82% and 73% in absolute ethanol and *n*-hexane, respectively. The presence of BG in the scaffold contributed to the increased

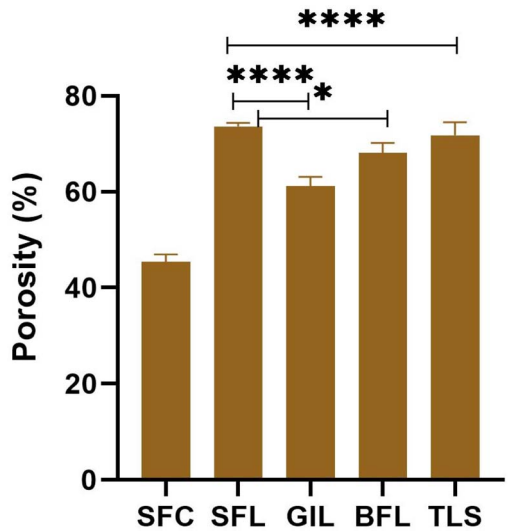

Fig. 8 % Porosity measurements of electrospun scaffolds in *n*-hexane. Error bars represent standard deviation ($n = 3$).

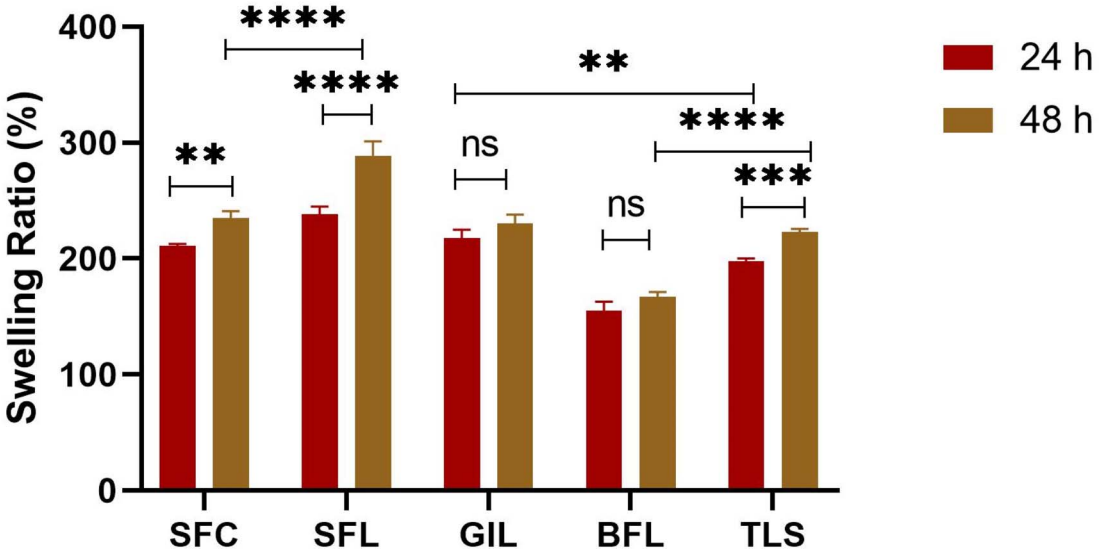

Fig. 9 Swelling ratio (%) of SFC, SFL, GIL, BFL and TLS scaffolds measured in PBS (pH 7.4) over 24 and 48 hours. Error bars represent standard deviation ($n = 3$).

porosity value for SF. In absolute ethanol, the percentage porosity for GIL, BFL and TLS was recorded as 65%, 56%, and 60%, respectively, while the porosity values for the same scaffolds in *n*-hexane were 61%, 68%, and 71%, respectively. The porosity of the SF material was initially 58% and it increased to 82% when BG was added to the SF to synthesize SFL. This increase occurred because the addition of BG particles created additional spaces between the silk fibers, leading to a higher porosity. The size and distribution of the BG particles affected the arrangement of the silk fibers, causing gaps to form and contribute to the overall increase in porosity. Additionally, the interaction between BG and SF was found to be weak, as indicated by FTIR results, resulting in lower affinity between the two materials and contributing to the creation of void spaces in the scaffold. On the other hand, incorporating OEO into PU decreased the porosity of the BFL from 65% to 56%. This decrease could be attributed to the hydrophobic nature of the OEO spheres, which increased the fiber diameter, thereby reducing porosity. Furthermore, OEO was observed to reduce the swelling behavior of the PU fibers, limiting fluid absorption and overall porosity. The volatile components of OEO also evaporated quickly during the electrospinning process, leading to faster drying of the fibers and reducing the formation of void spaces, ultimately decreasing the overall porosity of the electrospun sheet.[48] Upon examining the porosity of the TLS sample scaffold, it was found to be approximately 60%. This porosity was a result of the SFL, GIL, and BFL layers combined, similar to the porosity of the BFL scaffold. It was observed that stacking these layers caused some void spaces to be partially filled, and the adhesion between the layers provided structural stability, limiting the formation of pores and overall porosity.

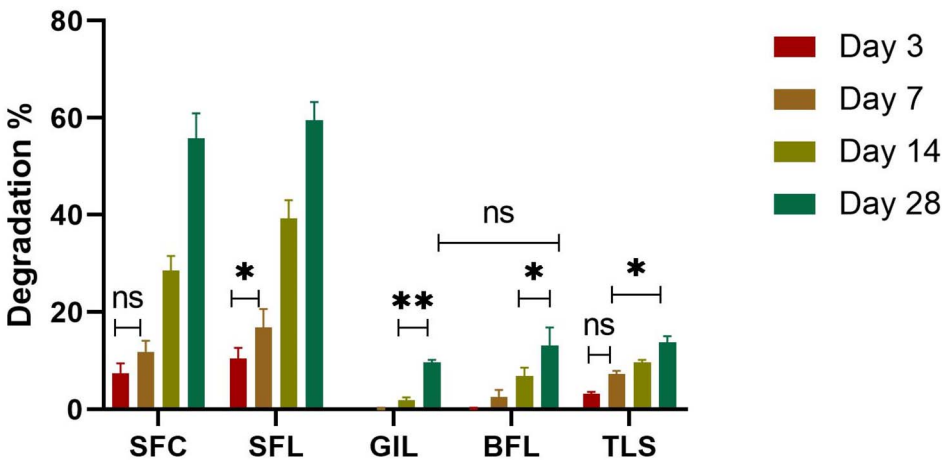

Fig. 10 *In vitro* degradation profile of SFC, SFL, GIL, BFL and TLS scaffolds after 3, 7, 14 and 28 days. Error bars represent standard deviation ($n = 3$).

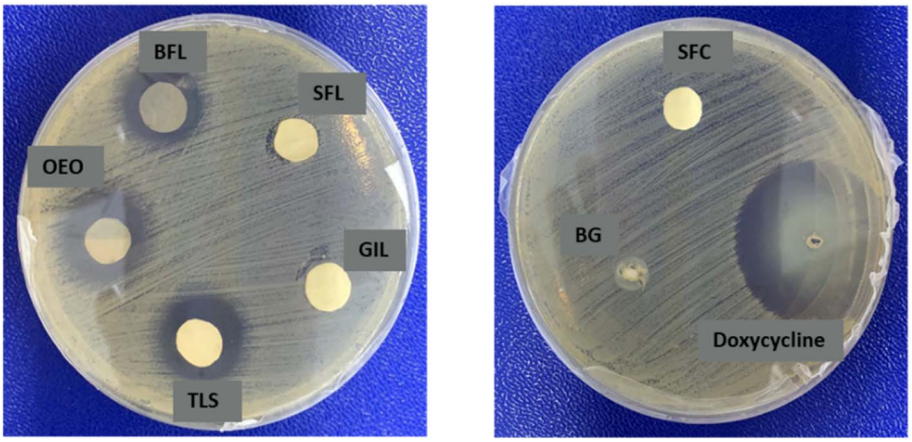

Fig. 11 Zone of inhibition of *Escherichia coli* growth after exposure to various scaffolds.

4.8 Swelling measurement

The water-absorbing ability of biomaterials significantly affects the maintenance of scaffolds and the growth of cells, important characteristics in tissue engineering and drug delivery systems.

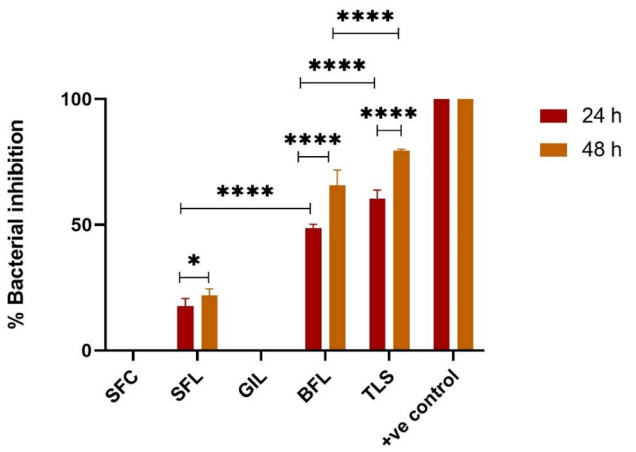

Fig. 12 Percentage bacterial inhibition of *Escherichia coli* after exposure to different scaffolds over 24 and 48 hours. Error bars represent standard deviation ($n = 3$).

The composition of biomaterials influences their water absorption ability. For example, scaffolds with hydrophilic groups exhibit a higher swelling rate, which allows them to absorb liquids and facilitate the passage of nutrients through the scaffold.[49] The swelling ratio of all scaffolds was measured in a PBS solution with a pH of 7.4 for 24 and 48 hours (Fig. 9). The results showed that the values increased with the duration of time. The recorded values at 24 hours were 211%, 238%, 218%, 155% and 164% for SFC, SFL, GIL, BFL and TLS, respectively, showing a gradual increase at 48 hours. Notably, the SFL mat exhibited the highest swelling percentage at approximately 238% due to its hydrophilic nature reflected by its contact angle value. The high swelling in the BG scaffolds could be attributed to its increased wettability. The presence of BG in SFL helped with water absorption and was important for the swelling process. This difference could impact cell adhesion and the deposition of proteins, potentially affecting tissue regeneration. Moreover, the addition of OEO to PU for the creation of BFL reduced its swelling from 218% to 155% probably due to the hydrophobic nature of OEO. The TLS composite scaffold showed a swelling percentage of 197%, owing to the additive effect of SFL, GIL and BFL; suitable for nutrient and oxygen transfer to promote cell attachment and growth.

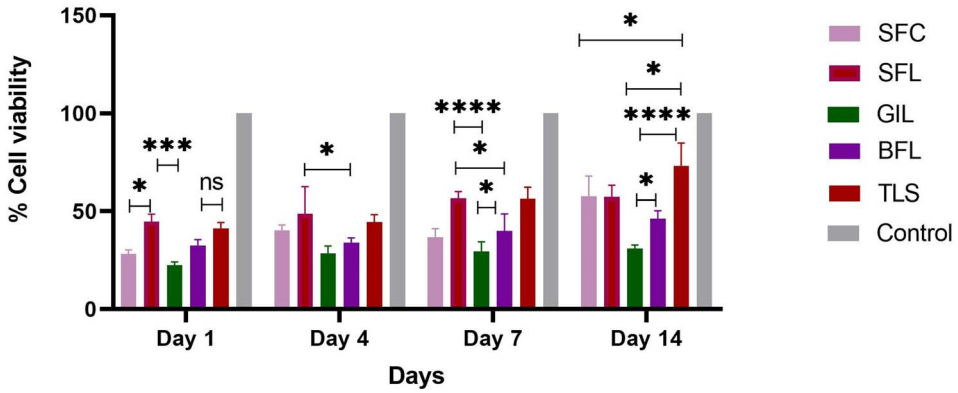

Fig. 13 Percentage cell viability of SFC, SFL GIL, BFL and TLS scaffolds. Error bars represent standard deviation ($n = 3$).

Swelling of biomaterials is an important factor in tissue engineering, as excessive swelling can impact the mechanical strength of scaffolds. Therefore, scaffolds should possess appropriate swelling for tissue engineering purposes.[30]

4.9 *In vitro* degradation study

Controlling biodegradation is essential in tissue engineering to enhance the effectiveness of the scaffold and guarantee that it aligns with the desired processes of tissue growth and regeneration.[50] Therefore, it is essential to adjust the degradation of the synthesized scaffolds to align with the appropriate tissue regrowth period for damaged tissues.[30] Over time, the sample scaffolds SFC, SFL and TLS showed signs of degradation, as shown by the increasing percentage degradation values on the graph (Fig. 10). As the incubation time was extended, the composite scaffolds exhibited higher levels of degradation, indicating that the degradation of the scaffolds is dependent on time. The resulting degradation products could potentially enhance bioactivity, making the scaffold more attractive to cells. In our study, we carefully selected polymers that met our specific criteria for regenerating dura mater. The degradation rate of the scaffolds corresponded with the wettability and swelling of the samples. Scaffolds showing high hydrophilic character; SFC and SFL showed accelerated degradation. GIL,

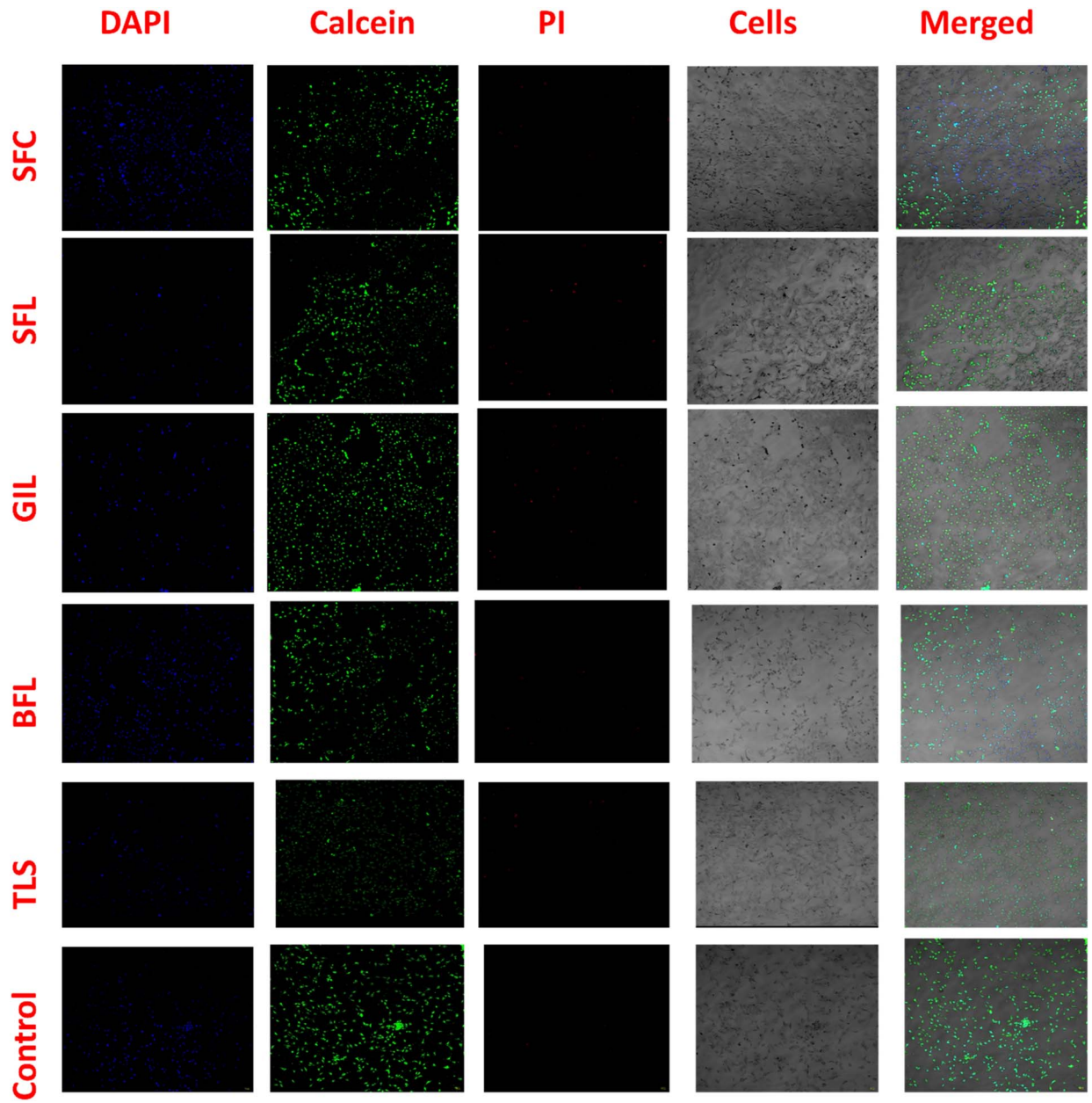

Fig. 14 Live-dead fluorescence microscopy images of fibroblast cells cultured on different electrospun scaffolds after 2 days of seeding. Calcein (green) indicates live cells and DAPI (blue) stains cell nuclei. All scaffolds supported cell attachment and proliferation with a few dead cells in some scaffolds. Notably, SFL and TLS scaffolds exhibited enhanced cell viability and higher fibroblast density, indicating favorable environments for cell growth and scaffold integration. The images were taken at 10×.

BFL and TLS exhibited a slow degradation compared to SFC and SFL scaffolds. The higher weight loss of SFC and SFL scaffolds was attributed to the increased wettability and swelling properties of these scaffolds. Initially, no weight loss was observed for GIL scaffolds in the first 7 days. However, slight degradation was noted at day 14 which increased at day 28. The less weight loss in GIL and BFL may be attributed to the hydrophobic character of the layers. The TLS material demonstrated a 13% optimal degradation rate within 28 days. The overall degradation of the composite scaffold is well-suited for maintaining long-term stability of the BFL, while providing a controlled environment to prevent cerebrospinal fluid leakage and suppress cancer cell growth. Furthermore, the SFL demonstrated remarkable degradation, which led to the formation of apatite from BG that supports skull fusion, as well as the generation of amino acids that promote dura mater regeneration by enhancing collagen production.

4.10 Antibacterial analysis

In this research, we investigated the effectiveness of synthesized samples against the Gram-negative bacterium, *Escherichia coli* using both disk diffusion and broth dilution method. In the disk diffusion method, pure OEO loaded on a UV-cured filter paper disk served as the negative control, while the commercial drug doxycycline poured on sterile filter paper was used as the positive control. The results showed that all samples except GIL exhibited antibacterial activity against *E. coli*. The zone of inhibition was found to be 5 mm ± 0.01 mm for SFL, 17 mm ± 0.01 mm for BFL, 18.8 mm ± 0.01 mm for TLS, 20 mm ± 0.01 mm for the negative control, and 27 mm ± 0.01 mm for the positive control. TLS demonstrated the highest activity, while SFL showed minimal inhibitory effect as shown in Fig. 11. In the broth dilution assay, the antibacterial activity was determined after 24 and 48 hours at 550–650 nm. The BFL scaffolds caused a gradual decrease in bacterial viability after 24 and 48 hours of incubation. During the first 24 hours, the percentage of bacterial inhibition was determined for the selected samples and found to be 17%, −26%, 48%, 60%, and 100% for SFL, GIL, BFL, TLS, and the positive control, respectively. The antibacterial efficiency increased over time for SFL, BFL and TLS, reaching values of 22%, 65%, and 80%, respectively (Fig. 12). The antibacterial effect was found to increase from SFL and BFL to TLS. BFL demonstrated excellent bacterial inhibition compared to SFL. The results indicated that adding BG enhanced the overall antibacterial activity of the TLS compared to the BFL and SFL scaffolds used alone. The antibacterial effect of SFL may be attributed to the release of Sr ions from the scaffold which inhibits cell wall synthesis, bacterial growth and reproduction, cell metabolism and chromosomal replication.[51] The antibacterial activity of oregano essential oil is attributed to the production of ROS as well as the presence of compounds like carvacrol, thymol and *p*-cymene, which ultimately lead to bacterial cell death.[52] The combination of OEO and BG in a composite scaffold demonstrated a synergistic effect, enhancing their individual antimicrobial properties. This resulted in a more powerful antibacterial effect, particularly effective against *E. coli*, a major cause of infections at injury sites. Therefore, it can be concluded that composite scaffolds have the potential to efficiently provide antibacterial protection against *E. coli* strains.

4.11 Cell viability

The materials used for scaffolding in tissue engineering are usually created to support cell growth, maintain normal cell differentiation and encourage proper physiological function.[53] Cell viability on all the scaffolds was evaluated by Alamar blue assay on days 1, 4, 7 and 14. At day 1, highest cell viability was seen in SFL (44%) and TLS (41%) scaffolds. The highest cell viability in the SFL scaffold can be attributed to the enhanced wettability of the SFL scaffold.[54] Cell proliferation in GIL scaffold at day 1 was evidently lower than the rest of the scaffolds and was approximately 22%. This can be explained by the fact

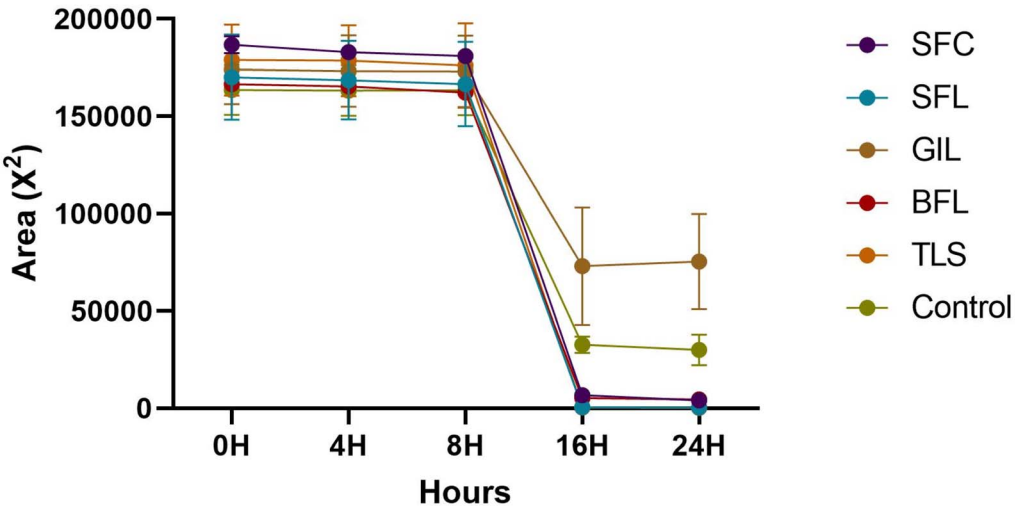

Fig. 15 Graph showing the scratch area (X^2) after different time intervals. Error bars represent standard deviation ($n = 3$). Some error bars are shorter than the size of the symbols.

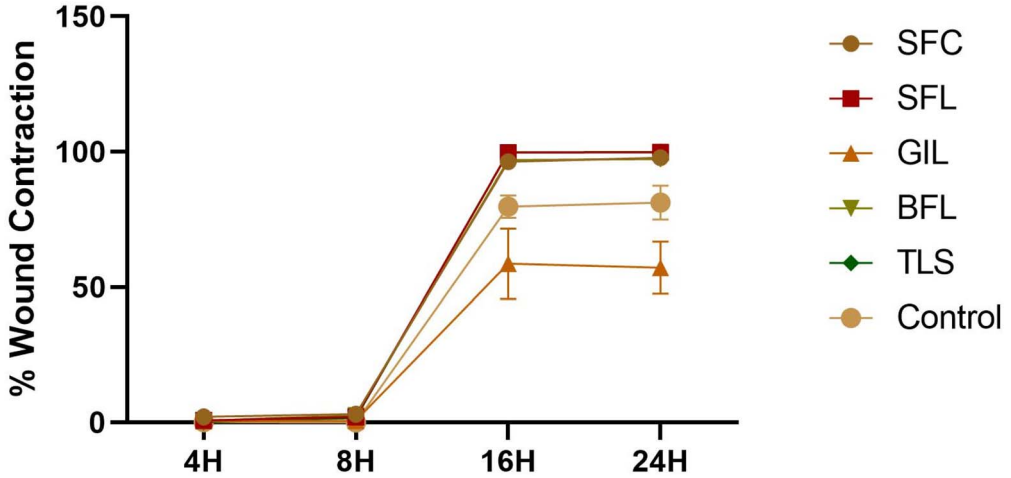

Fig. 16 % Wound contraction in SFC, SFL, GIL, BFL, TLS and control after different time intervals. Error bars represent standard deviation ($n = 3$). Some error bars are shorter than the size of the symbols.

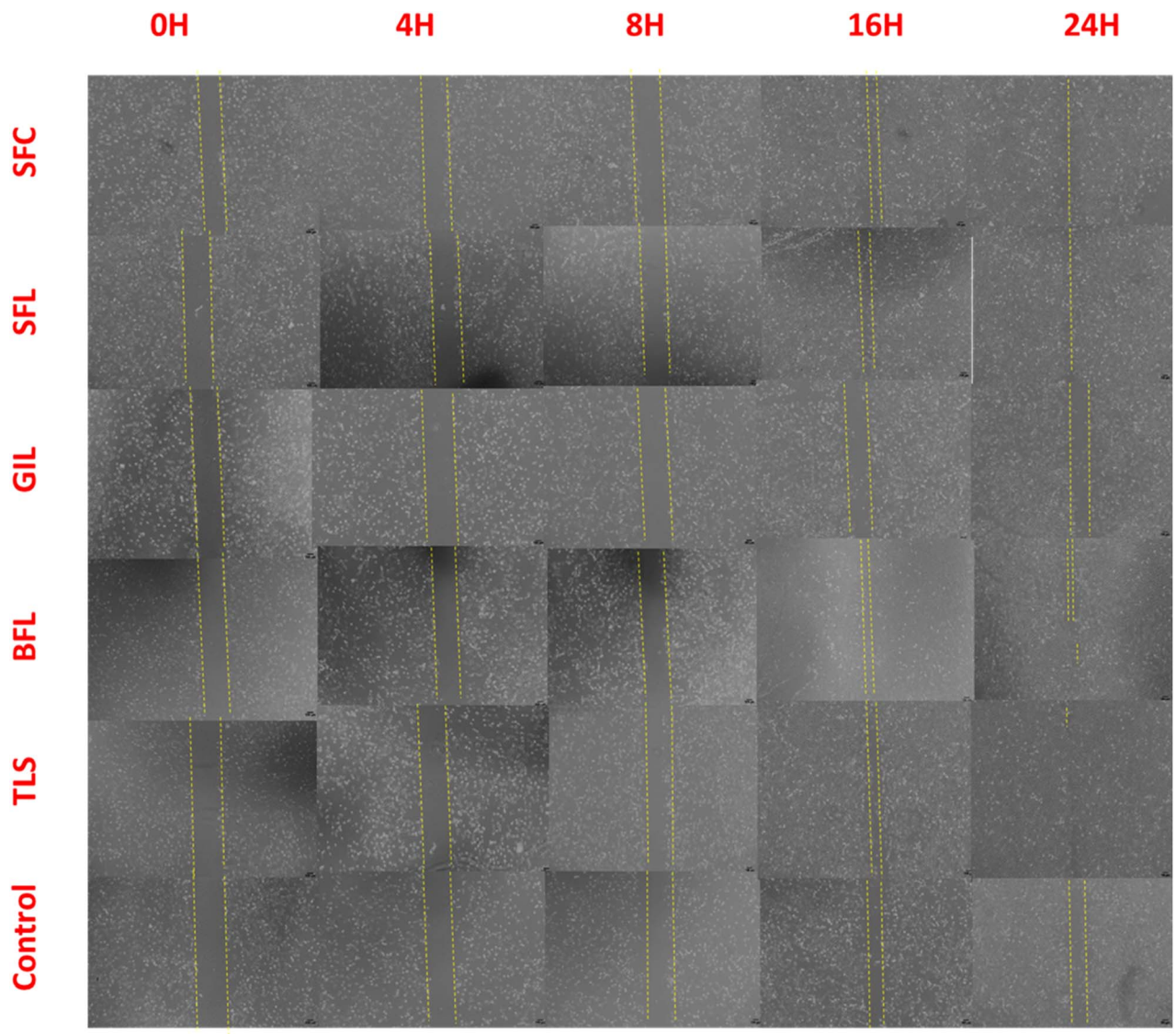

Fig. 17 Time-lapse images of scratch closure in the presence of synthesized scaffolds (SFC, SFL, GIL, BFL, TLS) and control over 0, 4, 8, 16 and 24 hours. Minimal cell migration was observed at early time points (4–8 h), while significant scratch closure occurred by 16 hours in SFC, SFL, BFL and TLS. After 24 hours, SFL and TLS achieved 99% scratch contraction, BFL 97% and GIL showed the least contraction (57.18%). These results demonstrate the excellent biocompatibility of synthesized scaffolds.

that PU is a synthetic polymer and its low biocompatibility has also been reported in the literature.[55] Effectiveness of PU scaffolds based on natural oils and polyols has been reported in literature.[56] Our results show that the cell viability of the SFL scaffold was significantly higher than the SFC scaffold at day 1. This suggests that the addition of Sr-based bioactive glass in SF promotes the proliferation of NIH/3T3 fibroblast cells. Research has shown that strontium can speed up the regrowth and development of bone by encouraging the transformation of osteoblasts, while also decreasing bone breakdown by impeding the formation of osteoclasts.[57,58] However, at day 14, the percentage cell viability of SFC increased and became approximate to SFL scaffold. As shown in Fig. 13, cell proliferation increased along with culture time which shows the biocompatible nature of the synthesized scaffolds. The results demonstrate that the scaffold containing SF can promote cell proliferation and adhesion which is also in agreement with previous results.[59,60] With time, cell viability increased and the highest viability was noted for TLS scaffold at day 14. The possible reason was the synergic effect of polymer matrix including SF, Sr-doped BG, PU and OEO which were exposed to the cells on the surface of scaffolds with time. The increased viability at day 14 for all the scaffolds confirms that cells are metabolically active and the scaffolds are biocompatible. Similar results were reported by other researchers.[61] Overall, the results show that the scaffolds are not toxic and support fibroblast proliferation and viability which is suitable for dura mater regeneration.

4.12 Live-dead assay

Live-dead analysis was performed to confirm the presence of live and dead cells as they interact with electrospun scaffolds. The results are shown in Fig. 14. All scaffolds were observed to support cell proliferation and growth after 2 days of seeding and a few dead cells were observed in some scaffolds. The viability of cells was prominent in SFL and TLS scaffolds after 2 days and a noticeably high number of fibroblast cells was seen in these scaffolds. DAPI and calcein staining showed that cells proliferated inside the architecture of all scaffolds which suggests that with time fibroblast cells can grow in the spaces of scaffolds and will replace the scaffolds with native extracellular matrix. The live-dead assay confirmed the high capability of all the scaffolds for cell viability and proliferation.

4.13 Scratch assay

The migration of fibroblast cells in the presence of synthesized scaffolds was assessed using *in vitro* cell migration assay (Fig. 15). Fig. 17 shows microscopic images of the samples and the control at 0, 4, 8, 16 and 24 hours. The figure reveals that there was no significant migration of cells in the presence of scaffolds or control after 4 and 8 hours. However, after 16 hours, a significant scratch contraction was observed in SFC, SFL, BFL and TLS as compared to control. After 24 hours, 99% scratch contraction was observed in SFL and TLS as depicted in Fig. 16. BFL showed 97% contraction whereas the slowest contraction (57.18%) was observed in GIL after 24 hours. Significant scratch closure was obtained in SFL, TLS and BFL, indicating good biocompatibility of synthesized scaffolds.

5 Conclusion

In the present study, a biomimetic trilayered scaffold (TLS) composed of electrospun silk fibers was developed for the purpose of dura mater regeneration. This scaffold is meticulously designed with three distinct layers with bioactive surfaces that accurately replicate the structural attributes of the dura mater. The external layer, facing the skull, integrates strontium-doped bioactive glass, while the internal layer, oriented towards the brain, incorporates oregano essential oil (OEO), with an inert layer positioned between the two to provide a protective barrier. The electrospun TLS exhibits optimal wettability, controlled *in vitro* degradation and favorable swelling characteristics that enhance cell proliferation and promote attachment to surrounding tissues. The inclusion of strontium-doped bioactive glass and OEO contributes to the thermal stability of the TLS while imparting significant antibacterial properties, thus offering additional protection against microbial infections. Results from *in vitro* cell culture assessments indicate that the fabricated trilayered scaffold significantly supports NIH3T3 cell attachment and promotes cellular proliferation. The synthetic trilayered electrospun scaffold introduced in this study effectively addresses the clinical need for an advanced dural substitute, facilitated by its superior physicochemical and biocompatible properties. Collectively, the findings highlight the promising potential of the TLS for effective dura mater regeneration.

Data availability

Data for this article including prism files of original graphs are available at google drive. **https://drive.google.com/file/d/19H3a1LAFk39I1w1Pu38hcP2L34t5RN5P/view?usp=sharing**.

Conflicts of interest

There are no conflict to declare.

Acknowledgements

Pakistan Science Foundation (PSF) is acknowledged for the award of a project under PSF-TUBITAK Joint initiative (PSF/TUBITAK/Biomedics/P/COMSATS (21)) to Dr Hamad Khalid. The authors Fahad Hussain Alhamoudi and H. Akhtar extend their appreciation to the Deanship of Scientific Research at King Khalid University for funding through Large Group Project under the grant number (RGP.2/555/45). Ather F Khan and Aqif A. Chaudhary are thankful to the Higher Education Commission of Pakistan for NRPU grant 15836.

References

1 F. Esposito, *et al.*, Collagen-only biomatrix as a novel dural substitute: examination of the efficacy, safety and outcome:

clinical experience on a series of 208 patients, *Clin. Neurol. Neurosurg.*, 2008, **110**(4), 343–351.
2 K. E. Flanagan, *et al.*, Development of a sutureless dural substitute from Bombyx mori silk fibroin, *J. Biomed. Mater.*, 2015, **103**(3), 485–494.
3 Y. Song, *et al.*, The pathological changes in the spinal cord after dural tear with and without autologous fascia repair, *Eur. Spine J.*, 2014, **23**(7), 1531–1540.
4 X. Bi, *et al.*, Applications of materials for dural reconstruction in pre-clinical and clinical studies: advantages and drawbacks, efficacy, and selections, *Mater. Sci. Eng.*, 2020, **117**, 111326.
5 X. W. Bi, *et al.*, Applications of materials for dural reconstruction in pre-clinical and clinical studies: advantages and drawbacks, efficacy, and selections, *Mater. Sci. Eng., C*, 2020, **117**, 111326.
6 T. Zhu, *et al.*, High efficacy of tetra-PEG hydrogel sealants for sutureless dural closure, *Bioact. Mater.*, 2022, **8**, 12–19.
7 D. E. Alekseev, E. D. Alekseev and D. V. Svistov, Comparative analysis of the efficiency of dura mater defect repair in cerebral surgery, *Zh. Vopr. Neirokhir. im. N. N. Burdenko*, 2018, **82**(5), 48–54.
8 A. Laun, J. C. Tonn and C. Jerusalem, Comparative study of lyophilized human dura mater and lyophilized bovine pericardium as dural substitutes in neurosurgery, *Acta Neurochir.*, 1990, **107**, 16–21.
9 A. Kinaci, *et al.*, Histologic comparison of the dura mater among species, *Comp. Med.*, 2020, **70**(2), 170–175.
10 D. Chauvet, *et al.*, Histological and biomechanical study of dura mater applied to the technique of dura splitting decompression in Chiari type I malformation, *Neurosurg. Rev.*, 2010, **33**, 287–295.
11 S. M. Barber, *et al.*, Cerebrospinal fluid leaks after spine tumor resection: avoidance, recognition and management, *J. Pharm. Health Care Sci.*, 2019, **7**(10), 217.
12 M. Protasoni, *et al.*, The collagenic architecture of human dura mater, *J. Neurosurg.*, 2011, **114**(6), 1723–1730.
13 W. Wang and Q. Ao, Research and application progress on dural substitutes, *J. Neurorestoratol.*, 2019, **7**(4), 161–170.
14 A. Kobayashi, *et al.*, Distinct origins of dura mater graft-associated Creutzfeldt-Jakob disease: past and future problems, *Acta Neuropathol. Commun.*, 2014, **2**(1), 1–8.
15 T. Mukai, *et al.*, Development of watertight and bioabsorbable synthetic dural substitutes, *Artif. Organs*, 2008, **32**(6), 473–483.
16 Y. Ramot, *et al.*, Local tolerance and biodegradability of a novel artificial dura mater graft following implantation onto a dural defect in rabbits, *Toxicol. Pathol.*, 2020, **48**(6), 738–746.
17 M. Pogorielov, *et al.*, Experimental evaluation of new chitin–chitosan graft for duraplasty, *J. Mater. Sci.*, 2017, **28**, 34.
18 P. K. Narotam, F. Qiao and N. Nathoo, Collagen matrix duraplasty for posterior fossa surgery: evaluation of surgical technique in 52 adult patients, *J. Neurosurg.*, 2009, **111**(2), 380–386.
19 S. Jin, *et al.*, A double-layer dura mater based on poly(caprolactone-co-lactide) film and polyurethane sponge: preparation, characterization, and biodegradation study, *J. Mater. Chem.*, 2021, **9**(18), 3863–3873.
20 L. Khorasani, *et al.*, Histological analysis of DuraGen in a human subject: case report, *Clin. Neuropathol.*, 2008, **27**(5), 361–364.
21 T. Ni, *et al.*, 3D bioprinting of bone marrow mesenchymal stem cell-laden silk fibroin double network scaffolds for cartilage tissue repair, *Bioconjugate Chem.*, 2020, **31**(8), 1938–1947.
22 S. Yodmuang, *et al.*, Silk microfiber-reinforced silk hydrogel composites for functional cartilage tissue repair, *Acta Biomater.*, 2015, **11**, 27–36.
23 V. P. Ribeiro, *et al.*, Enzymatically cross-linked silk fibroin-based hierarchical scaffolds for osteochondral regeneration, *ACS Appl. Mater. Interfaces*, 2019, **11**(4), 3781–3799.
24 Y. Wang, *et al.*, In vivo degradation of three-dimensional silk fibroin scaffolds, *Biomaterials*, 2008, **29**(24–25), 3415–3428.
25 Z. Mao, *et al.*, A Cell-Free Silk Fibroin Biomaterial Strategy Promotes In Situ Cartilage Regeneration Via Programmed Releases of Bioactive Molecules, *Adv. Healthcare Mater.*, 2023, **12**(1), 2201588.
26 P. Chen, *et al.*, Towards Highly Matching the Dura Mater: A Polyurethane Integrating Biocompatible, Leak-Proof, and Self-Healing Properties, *Macromol. Biosci.*, 2023, 2300111.
27 M. Montazerian and E. D. Zanotto, Bioactive and inert dental glass-ceramics, *J. Biomed. Mater. Res.*, 2017, **105**(2), 619–639.
28 H. Khalid, *et al.*, Silk fibroin/collagen 3D scaffolds loaded with TiO2 nanoparticles for skin tissue regeneration, *Polym. Bull.*, 2021, **78**, 7199–7218.
29 A. U. R. Khan, *et al.*, Physico-chemical and biological evaluation of PLCL/SF nanofibers loaded with oregano essential oil, *Pharmaceutics*, 2019, **11**(8), 386.
30 P. Reardon, *et al.*, Mimicking hierarchical complexity of the osteochondral interface using electrospun silk-bioactive glass composites, *ACS Appl. Mater. Interfaces*, 2017, **9**(9), 8000–8013.
31 B. Li, *et al.*, A solvent system involved fabricating electrospun polyurethane nanofibers for biomedical applications, *Polymers*, 2020, **12**(12), 3038.
32 F. Plati, R. Papi and A. Paraskevopoulou, Characterization of oregano essential oil (Origanum vulgare L. subsp. hirtum) particles produced by the novel nano spray drying technique, *Foods*, 2021, **10**(12), 2923.
33 K. Kurpinski and S. Patel, Dura mater regeneration with a novel synthetic, bilayered nanofibrous dural substitute: an experimental study, *Nanomedicine*, 2011, **6**(2), 325–337.
34 I. L. Liakos, *et al.*, Electrospun fiber pads of cellulose acetate and essential oils with antimicrobial activity, *Nanomaterials*, 2017, **7**(4), 84.
35 M. Zhao, *et al.*, Chemical, thermal, time, and enzymatic stability of silk materials with silk I structure, *Int. J. Mol. Sci.*, 2021, **22**(8), 4136.
36 K. Kawase, *et al.*, Changes in essential oil of Origanum vulgare L. affected by different extraction methods, *Int. J. Recent Res. Appl. Stud.*, 2013, **14**, 238.

37 D. Filip, D. Macocinschi and S. Vlad, Thermogravimetric study for polyurethane materials for biomedical applications, *Composites, Part B*, 2011, **42**(6), 1474–1479.
38 S. El Baakili, K. El Mabrouk and M. Bricha, Acellular bioactivity and drug delivery of new strontium doped bioactive glasses prepared through a hydrothermal process, *RSC Adv.*, 2022, **12**(24), 15361–15372.
39 G. M. Campbell and A. Sophocleous, Quantitative analysis of bone and soft tissue by micro-computed tomography: applications to ex vivo and in vivo studies, *BoneKEy Rep.*, 2014, **3**, 564.
40 M. R. Bidgoli, *et al.*, Fabrication of hierarchically porous silk fibroin-bioactive glass composite scaffold via indirect 3D printing: effect of particle size on physico-mechanical properties and in vitro cellular behavior, *Mater. Sci. Eng.*, 2019, **103**, 109688.
41 S. K. Jaganathan, *et al.*, Biomimetic electrospun polyurethane matrix composites with tailor made properties for bone tissue engineering scaffolds, *Polym. Test.*, 2019, **78**, 105955.
42 R. Schmidmaier and P. Baumann, ANTI-ADHESION evolves to a promising therapeutic concept in oncology, *Curr. Med. Chem.*, 2008, **15**(10), 978–990.
43 A. Chandrasekaran, *et al.*, Physico-chemical and biological studies on three-dimensional porous silk/spray-dried mesoporous bioactive glass scaffolds, *Ceram. Int.*, 2016, **42**(12), 13761–13772.
44 A. S. Lin, *et al.*, Microarchitectural and mechanical characterization of oriented porous polymer scaffolds, *Biomaterials*, 2003, **24**(3), 481–489.
45 M. N. Khan, J. M. M. Islam and M. A. Khan, Fabrication and characterization of gelatin-based biocompatible porous composite scaffold for bone tissue engineering, *J. Biomed. Mater. Res.*, 2012, **100**(11), 3020–3028.
46 R. Abbe, Rubber tissue for meningeal adhesions, *Trans. Am. Surg. Assoc.*, 1895, (13), 490–491.
47 S. Srinivasan, *et al.*, Biocompatible alginate/nano bioactive glass ceramic composite scaffolds for periodontal tissue regeneration, *Carbohydr. Polym.*, 2012, **87**(1), 274–283.
48 K. Duan, *et al.*, A novel high mechanical and excellent hydrophilic electrospun polyurethane-silk-bioactive glass nanofiber film for rotator cuff injury repair, *J. Appl. Polym. Sci.*, 2022, **139**(10), 51746.
49 D. Archana, *et al.*, Chitosan-pectin-alginate as a novel scaffold for tissue engineering applications, *Indian J. Biotechnol.*, 2013, **12**, 475–482.
50 L. Zhang, *et al.*, Tailoring degradation rates of silk fibroin scaffolds for tissue engineering, *J. Biomed. Mater. Res.*, 2019, **107**(1), 104–113.
51 N. Baheiraei, *et al.*, Effects of strontium ions with potential antibacterial activity on in vivo bone regeneration, *Sci. Rep.*, 2021, **11**(1), 8745.
52 K. Luo, *et al.*, Antibacterial effect of oregano essential oil against Vibrio vulnificus and its mechanism, *Foods*, 2022, **11**(3), 403.
53 K. Zhang, *et al.*, Electrospun scaffolds from silk fibroin and their cellular compatibility, *J. Biomed. Mater. Res. A.*, 2010, **93**(3), 976–983.
54 X. Liu and P. X. Ma, Polymeric scaffolds for bone tissue engineering, *Ann. Biomed. Eng.*, 2004, **32**, 477–486.
55 H.-s. Park, *et al.*, Silk fibroin–polyurethane blends: Physical properties and effect of silk fibroin content on viscoelasticity, biocompatibility and myoblast differentiation, *Acta Biomater.*, 2013, **9**(11), 8962–8971.
56 S. K. Jaganathan, *et al.*, Fabrication and characterisation of nanofibrous polyurethane scaffold incorporated with corn and neem oil using single stage electrospinning technique for bone tissue engineering applications, *J. Polym. Res.*, 2018, **25**, 1–12.
57 J. Braux, *et al.*, A new insight into the dissociating effect of strontium on bone resorption and formation, *Acta Biomater.*, 2011, **7**(6), 2593–2603.
58 X.-y. Zhang, *et al.*, Biocompatiable silk fibroin/carboxymethyl chitosan/strontium substituted hydroxyapatite/cellulose nanocrystal composite scaffolds for bone tissue engineering, *Int. J. Biol. Macromol.*, 2019, **136**, 1247–1257.
59 J. Du, *et al.*, Potential applications of three-dimensional structure of silk fibroin/poly(ester-urethane) urea nanofibrous scaffold in heart valve tissue engineering, *Appl. Surf. Sci.*, 2018, **447**, 269–278.
60 J. Lv, *et al.*, Promoting epithelium regeneration for esophageal tissue engineering through basement membrane reconstitution, *ACS Appl. Mater. Interfaces*, 2014, **6**(7), 4954–4964.
61 M. Samie, *et al.*, Fabrication of dual drug loaded bilayered chitosan based composite scaffolds as osteochondral substitutes and evaluation of in vitro cell response using the MC3T3 pre-osteoblast cell line, *Cellulose*, 2020, **27**, 2253–2266.